

Damping mechanisms of high-lying single-particle states in ^{91}Nb

H. K. T. van der Molen,¹ H. Akimune,² A. M. van den Berg,¹ I. Daito,² H. Fujimura,² Y. Fujita,³ M. Fujiwara,^{2,4} M. N. Harakeh,^{1,*} M. Hunyadi,^{1,†} F. Ihara,² T. Inomata,² K. Ishibashi,² J. Jänecke,⁵ N. Kalantar-Nayestanaki,¹ H. Laurent,⁶ I. Lhenry,⁶ T. W. O'Donnell,⁵ V. A. Rodin,^{1,7} A. Tamii,⁸ H. Toyokawa,⁹ M. H. Urin,^{1,7} H. Yoshida,² and M. Yosoi²

¹*Kernfysisch Versneller Instituut (KVI), University of Groningen, 9747 AA Groningen, The Netherlands*

²*Research Center for Nuclear Physics, Osaka University, Ibaraki, Osaka 567-0047, Japan*

³*Department of Physics, Osaka University, Toyonaka, Osaka 560-0043, Japan*

⁴*Advanced Science Research Center, JAERI, Tokai, Ibaraki 319-1195, Japan*

⁵*Department of Physics, University of Michigan, Ann Arbor, Michigan 48109-1040, USA*

⁶*Institut de Physique Nucléaire, IN2P3-CNRS, F-91406 Orsay Cedex, France*

⁷*Department of Theoretical Nuclear Physics, MEPI, RU-115409 Moscow, Russia*

⁸*Department of Physics, Kyoto University, Sakyo, Kyoto 606-8224, Japan*

⁹*SPring-8, Japan Synchrotron Research Institute, Hyogo 679-5198, Japan*

(Received 26 September 2006; published 18 January 2007)

Decay by proton emission from high-lying states in ^{91}Nb , populated in the $^{90}\text{Zr}(\alpha, t)$ reaction at $E_\alpha = 180$ MeV, has been investigated. Decay to the ground state and semidirect decay to the low-lying (2^+ , 5^- , and 3^-) phonon states in ^{90}Zr were observed. It was found that these phonon states play an important role in the damping process of the single-particle states. An optical-model coupled-channel approach was used successfully to describe the direct and semidirect parts of the decay.

DOI: [10.1103/PhysRevC.75.014311](https://doi.org/10.1103/PhysRevC.75.014311)

PACS number(s): 25.55.Hp, 23.50.+z, 21.10.Pc, 27.60.+j

I. INTRODUCTION

In the shell model, single-particle (s.p.) states are eigenstates of the Hamiltonian, and they have a narrow width if particle decay is forbidden. On the other hand, if the s.p. states are unbound to particle decay, they acquire a width (escape width Γ^\uparrow) due to coupling to the continuum. This escape width depends on a number of factors, i.e., the available decay energy, orbital angular momentum of the s.p. state, and height of the Coulomb barrier (if the emitted particle is charged, i.e., a proton). At high excitation energies, s.p. states, even those bound to particle decay, usually exhibit a giant-resonance-like structure. The width in this case (spreading width Γ^\downarrow) is acquired by coupling to the underlying, more complex configurations. The first step in this damping mechanism is mediated via coupling to a special class of particle-hole states, i.e., the surface vibrations [1,2]. In successive steps, these states with simple configurations couple to those with more complex ones. This finally leads to statistical decay at the end of the equilibration process, which is quite well described in the Hauser-Feshbach formalism (see Ref. [3]).

High-lying s.p. states have been studied by s.p. stripping reactions [4–8] and have been observed as broad giant-resonance-like structures superimposed on top of a nuclear continuum, the main source of which is breakup processes. In these studies, it was possible to determine some systematics of these high-lying s.p. states such as the excitation energies, spin and parity, total width, and depletion of the s.p. strength expected on the basis of a simple shell model. However, direct

information on the microscopic structure of these high-lying s.p. states and their damping mechanism is only obtained from their decay properties. These include in particular the particle decays to the ground state (g.s.) and to the low-lying collective states of the target nucleus, as well as to the continuum states of the target nucleus followed by particle decay to relevant daughter nuclei.

Such studies have been made for the decay of the high-lying s.p. neutron states of ^{209}Pb and some medium-weight nuclei [9–11]. In these studies, however, disentangling the statistical and direct and semidirect neutron decays to low-lying states is not straightforward, since the relative contributions depend very strongly on statistical-model calculations in the spirit of the Hauser-Feshbach formalism with its inherent uncertainties. The statistical-model calculations involve some ambiguities which can lead to difficulties in interpreting the experimental results against the theoretical calculations.

The present work aims to study the damping mechanisms of high-lying s.p. states in a medium-heavy nucleus through the measurement of decay by proton emission. We used the $^{90}\text{Zr}(\alpha, t)$ reaction to populate high-spin states in ^{91}Nb . The thresholds for proton and neutron emission are $S_p = 5.15$ MeV and $S_n = 12.05$ MeV, respectively. It should be noted that for a medium-heavy nucleus, neutron emission will be the dominant mode for statistical decay, once the neutron channel is open. In the present case in which proton-decay channels are being studied, the determination of the branching ratios for direct and semidirect proton decay from the experimental data is not hampered by large amounts of statistical proton decay. These branching ratios are, therefore, less affected by statistical-model calculations. Moreover, the detection of protons is relatively easy, and detection inefficiencies can be neglected, which is in contrast to the detection of neutrons. Using the (^7Li , ^6He) reaction,

*Corresponding author. Electronic mail: harakeh@kvi.nl

†Present address: Institute of Nuclear Research of the Hungarian Academy of Sciences, H-4001 Debrecen, Hungary.

Galès [9] has also studied high-spin states in ^{91}Nb . Similar to the present investigation, protons were measured in coincidence with ejectiles detected at a scattering angle of 0° . However, no information was obtained on the branching ratios for the decay from high-lying states to the phonon states in ^{90}Zr . Furthermore, the energy resolution in the ($^7\text{Li}, ^6\text{He}$) experiment was rather poor.

The theoretical framework for the calculations used to compare with the present $^{90}\text{Zr}(\alpha, t)$ data will be discussed in Sec. II. In Sec. III we will describe the experimental setup used and the reduction of the data obtained from the experiment. In Sec. IV, the experimental data and the results of the calculations will be discussed. Finally, the conclusions will be presented in Sec. V. The initial results of this experiment have been reported elsewhere [12]. Furthermore, the population and decay of isobaric analog states (IAS's), which were studied in the same experiment, have already been published [13].¹

II. THEORETICAL FRAMEWORK

A. Description of the theoretical model

In a potential scattering model, direct (D) and semidirect (SD) nucleon decay can be described as phenomena that differ only by the scattering of the particle from either the g.s. or the phonon state, respectively. The optical model and the coupled-channel approach, which is a generalized version of the optical model, are widely used to describe the scattering (see, e.g., Refs. [14,15]). Therefore, it is natural to use an optical-model coupled-channel (OMCC) approach to describe these phenomena. Such an approach has been developed in Refs. [16,17] to describe the direct neutron decay of high-spin quasibound single-neutron states in ^{209}Pb and ^{91}Zr to the g.s. and to low-lying collective (one-phonon) states of ^{208}Pb and ^{90}Zr , respectively. An attempt to describe these phenomena without the use of an OMCC approach was undertaken by Van Giai *et al.* [18]. The experimental data reported by Fortier *et al.* [11] were qualitatively described in Refs. [16,18]. An attempt to theoretically describe the decay of quasibound single-proton states in ^{91}Nb has been undertaken recently by Urin and Chekomazov [17]. However, the calculation was limited by the small number of single-proton states and by the rather high excitation-energy interval examined in ^{91}Nb . Furthermore, a schematic optical-model potential was used in that work. In the present calculations, we attempt to eliminate those shortcomings by (i) expanding the excitation-energy region for ^{91}Nb , (ii) considering all quasibound single-proton states in the excitation-energy region, and (iii) using a modern optical-model potential for the system $p\text{-}^{90}\text{Zr}$ described recently by Romanovsky *et al.* [19].

¹The single-, double- and triple-differential cross sections presented in Refs. [12] and [13] should be multiplied by a correction factor 3.0. This renormalization factor for the absolute cross sections has been determined from a recent measurement of the absolute cross sections of the g.s., $9/2^+$ and IAS, $11/2^-$ in ^{91}Nb in the $^{90}\text{Zr}(\alpha, t)$ reaction; see Sec. III A.

1. Single-particle strength

For a meaningful comparison of the observed direct and semidirect decay from s.p. states with theoretical values, it is also necessary to calculate the excitation cross sections for these states. In the calculation of the cross section for a certain reaction, one usually separates the nuclear structure part from the part that involves the reaction mechanism. For the case of an isolated level at an excitation energy ε populated in a stripping reaction, as in the present (α, t) reaction, the cross section can be written as

$$\frac{d\sigma_{lj}(\theta, \varepsilon)}{d\Omega} = N \frac{2J_f + 1}{2J_i + 1} C^2 S_{lj} \frac{\sigma_{lj}^{\text{DW}}(\theta, \varepsilon)}{2j + 1}. \quad (1)$$

Here, $\sigma_{lj}^{\text{DW}}(\theta, \varepsilon)$ is the part that describes the reaction mechanism. It can be calculated for a s.p. transfer with orbital and total angular momentum l and j , respectively, in the distorted-wave Born approximation (DWBA) using the code DWUCK [20]. In this equation, N is the factor needed to normalize the calculated cross section to the experimental one, and $C^2 S_{lj}$ is the spectroscopic factor with the isospin Clebsch-Gordan coefficient C . Furthermore, J_i and J_f are the spins of the g.s. of the target nucleus and the level populated in the final nucleus, respectively. When the g.s. of the target nucleus has $J_i = 0$, then $J_f = j$ and the spin factors cancel out, and the cross section simplifies to

$$\frac{d\sigma_{lj}(\theta, \varepsilon)}{d\Omega} = N \cdot C^2 S_{lj} \sigma_{lj}^{\text{DW}}(\theta, \varepsilon). \quad (2)$$

Experimentally, it is not always possible in the (α, t) reaction studied to unambiguously determine the spin of an observed state. In many cases, especially at higher excitation energies, the observed cross sections originate from the excitation of a number of overlapping s.p. states. As a result, the different contributions cannot be derived from the experimental data, and calculated cross sections have to be used:

$$\sigma^{\text{inc}}(\varepsilon) = N \sum_{lj} C^2 S_{lj}(\varepsilon) \cdot \Delta\varepsilon \cdot \sigma_{lj}^{\text{DW}}(\theta, \varepsilon). \quad (3)$$

Here, $S_{lj}(\varepsilon)$ is the spectroscopic strength function which describes the nuclear-structure part as a function of excitation energy ε , and $\Delta\varepsilon$ is the excitation-energy interval over which the s.p. strength is integrated. Because of the coupling to other states, the strength of a s.p. state is fragmented over many states, especially at higher excitation energies. Note that the s.p. Green's function contains all information on the damping of s.p. states. We use the optical-model approach [16] to evaluate the energy-averaged s.p. Green's function. Within this approach, the strength function of bound s.p. states can be calculated using the expression

$$S_{lj}(\varepsilon) = -\frac{1}{\pi} \int_0^\infty \text{Im} g_{lj}(r, r'; \varepsilon) dr. \quad (4)$$

Here, $(rr')^{-1} g_{lj}(r, r'; \varepsilon)$ is the radial part of the optical-model Green's function. In the vicinity of a s.p. state with energy $\varepsilon_0 < 0$, Green's function can be represented in the following form [21]:

$$g_{lj}(r, r'; \varepsilon) = \frac{\chi_{nlj}(r) \chi_{nlj}(r')}{\varepsilon - \varepsilon_0 + i\Gamma\downarrow/2}, \quad (5)$$

where $\chi_{nlj}(r)$ is the radial part of the s.p. bound wave function and Γ^\downarrow is the spreading width of the state. Substituting Eq. (5) into Eq. (4), one arrives at the usual expression for the s.p. strength function:

$$S_{nlj}(\varepsilon) = \frac{1}{2\pi} \frac{\Gamma_{lj}^\downarrow}{(\varepsilon - \varepsilon_0)^2 + \Gamma_{lj}^{\downarrow 2}/4}. \quad (6)$$

For positive energies ($\varepsilon > 0$), the integral in Eq. (4) formally diverges because of the nonvanishing value of the continuum wave function for $r \rightarrow \infty$. Nevertheless, in the vicinity of a quasibound s.p. state with energy $\varepsilon_0 > 0$, an approximate expression similar to Eq. (5) can be written for $r, r' \leq R$ [21]:

$$g_{lj}(r, r'; \varepsilon) = \frac{\chi_0(r)\chi_0(r')}{\varepsilon - \varepsilon_0 + i(\Gamma^\downarrow + \Gamma^\uparrow)/2}. \quad (7)$$

Here, $\chi_0(r)$ is normalized approximately to unity in the interval $r < R$, and Γ^\uparrow is the escape width of the s.p. resonance. In the actual calculation of the strength function, a cutoff radius R^* is used as the upper limit of the integral shown in Eq. (4), with R^* chosen to satisfy the condition $\int_0^{R^*} \chi_0^2(r) dr \approx 1$. Of course, R^* is chosen to be larger than the nuclear radius R . This procedure allows us to also use Eq. (4) for the calculation of the strength function of quasibound s.p. states; in this case, the cutoff parameter R^* replaces the upper limit in this integral.

2. Direct decay to the ground state

Let $\sigma_{lj}^{\text{inc}}(\varepsilon)$ be the energy-averaged inclusive cross section for a one-proton transfer reaction with given values of the energy ε and total and orbital angular momenta j and l , respectively. Furthermore, let $\sigma_{lj,0^+}^{\text{D}}(\varepsilon)$ denote the direct part of the energy-averaged partial decay cross section, corresponding to the population of the 0^+ g.s. of a (double-even) target nucleus, which in the present case is ^{90}Zr . The inclusive cross section can be expressed in terms of an ordinary optical model and a vertex function $f_{lj}(r, \varepsilon)$, which is, generally speaking, unknown and depends on the reaction considered. From Refs. [16,17] we find that

$$\sigma_{lj}^{\text{inc}}(\varepsilon) \sim -\frac{1}{\pi} \text{Im} \int f_{lj}^*(r, \varepsilon) g_{lj}(r, r'; \varepsilon) f_{lj}(r', \varepsilon) dr dr' \quad (8)$$

and

$$\sigma_{lj,0^+}^{\text{D}}(\varepsilon) \sim \left| \int f_{lj}(r, \varepsilon) \chi_{\varepsilon lj}^{(+)}(r) dr \right|^2, \quad (9)$$

where $r^{-1} \chi_{\varepsilon lj}^{(+)}(r)$ is the radial part of the optical-model continuum wave function for the proton. This function is normalized such that both cross sections are the same in the 'potential' limit ($W \rightarrow 0$), where the spreading effect can be neglected. In the vicinity of the single-proton state $\{l, j\}$, the branching ratio for the decay to the g.s. of the daughter (target) nucleus is independent of the vertex function f_{lj} and has the simple form [16,17]

$$b_{lj,0^+}^{\text{D}}(\varepsilon) = \frac{\sigma_{lj,0^+}^{\text{D}}(\varepsilon)}{\sigma_{lj}^{\text{inc}}(\varepsilon)} \longrightarrow \frac{\Gamma_{lj,0^+}^\uparrow(\varepsilon)}{\Gamma_{lj}^\downarrow(\varepsilon)}, \quad (10)$$

where Γ^\uparrow and Γ^\downarrow are the s.p. escape and spreading widths, respectively. It is assumed that $\Gamma^\uparrow \ll \Gamma^\downarrow$.

3. Semidirect decay to phonon states

The semidirect part of the decay cross section can be calculated within the coupled-channel approach assuming that the particle-phonon coupling is weak [16,17]:

$$\sigma_{lj,L^\pi}^{\text{SD}}(\varepsilon) \sim \sum_{l'j'} \left| \int f_{lj}(r, \varepsilon) g_{lj}(r, r'; \varepsilon) v_L(r') \chi_{\varepsilon' l' j'}^{(+)}(r') dr dr' \right|^2 \times \eta_L(lj, l'j'). \quad (11)$$

Here, $\eta_L(lj, l'j') \equiv \langle lj \| Y_L \| l'j' \rangle^2 / (2j+1)$ is the kinematic factor, $\varepsilon' = \varepsilon - \omega_L$ with ω_L the phonon energy, and L^π is the one-phonon angular momentum and its associated parity. We use the phenomenological one-phonon transition potential $v_L(r)$ which is often used in the coupled-channel approach:

$$v_L(r) = \frac{1}{\sqrt{2L+1}} \beta_L R \frac{\partial U(r)}{\partial r}, \quad (12)$$

where β_L is the dynamic-deformation parameter and $U(r)$ is the central part of the nuclear mean field for protons. A description of the potential and the dynamic deformation parameters used in the present analysis is given in Sec. II B 1. Similar to Eq. (10), our definition of the branching ratio for the semidirect decay of the s.p. state $\{l, j\}$ to the one-phonon state of the product nucleus is

$$b_{lj,L^\pi}^{\text{SD}}(\varepsilon) = \frac{\sigma_{lj,L^\pi}^{\text{SD}}(\varepsilon)}{\sigma_{lj}^{\text{inc}}(\varepsilon)} \longrightarrow \frac{\Gamma_{lj,L^\pi}^{\downarrow\uparrow}(\varepsilon)}{\Gamma_{lj}^\downarrow(\varepsilon)}, \quad (13)$$

where $\Gamma^{\downarrow\uparrow}$ represents the semidirect decay width. Again, in the vicinity of a quasibound state $\{l, j\}$, this branching ratio is equal to the ratio of corresponding widths [16,17]. In transfer-reaction experiments leading to the population of states in the continuum, cross sections summed over all available values for l and j are measured. Therefore, only the integral ratio b_{L^π} can be compared with the theoretical estimates given as

$$b_{L^\pi}(\varepsilon) = \frac{\sum \sigma_{lj,L^\pi}^{\text{D,SD}}(\varepsilon)}{\sum \sigma_{lj}^{\text{inc}}(\varepsilon)} = \sum b_{lj,L^\pi}^{\text{D,SD}}(\varepsilon) w_{lj}(\varepsilon), \quad (14)$$

where L^π includes the g.s. with 0^+ , and $w_{lj}(\varepsilon)$ is the relative probability for the excitation of the $\{l, j\}$ -state

$$w_{lj}(\varepsilon) = \sigma_{lj,L^\pi}^{\text{inc}}(\varepsilon) / \sum \sigma_{lj}^{\text{inc}}(\varepsilon). \quad (15)$$

These probabilities can be calculated using DWBA, provided that the s.p. strength functions $S_{lj}(\varepsilon)$ are known as described in Sec. II A 1.

4. Angular correlations

The angular correlation between a decay particle and an ejectile is determined by the quantum numbers and the magnetic substate population amplitudes of the intermediate state of the decaying nucleus and the spin and orbital angular momenta carried by the decay particle. When only one intermediate state is populated in the nucleus and subsequent particle decay occurs to a 0^+ state, like the g.s. in ^{90}Zr , only one l value is allowed; therefore, the unknown J^π of the intermediate state can be determined uniquely from the angular correlation of the decay particle. In the case of a nonzero spin of the target nucleus, a number of transfer angular momenta may contribute. When the solid angle of the ejectile detector is finite and the associated spin transfer is not zero, more than one magnetic substate will be populated. Furthermore, when the final state is not a 0^+ state, various combinations of $\{l, j\}$ for the decay particle are possible. Finally, if two or more intermediate overlapping states are involved in the decay process, the contributions of these states should be added coherently.

The angular correlation functions were calculated using the program ANGCOR [22]. This program takes into account the finite solid angle for both ejectile and decay-particle detectors. The m -state population of the intermediate state is obtained from the DWBA program DWUCK [20]. Although more than two l values can be taken into account using ANGCOR, only two l values were used in the calculation, because it can be assumed that only the lowest values of l give a significant contribution. Decay with larger l values is suppressed by the centrifugal barrier. The calculated theoretical angular correlations $W(\theta)$ can be fitted to the experimental data using a χ^2 minimization. This yields the partial cross sections for the decay from the excited state to the final state, provided that the correlation functions are normalized properly.

Interference between states with opposite parity gives rise to angular correlations which are not symmetric around 90° . Different angular correlations, with similar shapes at (backward) angles where the detectors were located but rather different shapes at other (forward) angles, can give rise to significantly different cross sections integrated over θ from 0 to π . It is, therefore, important to take these interference effects into account. This effect is especially important in the decay to the 0^+ g.s., because a few s.p. decays can contribute. The angular correlations for decay to higher-lying states are more isotropic.

B. Input parameters for the calculations

1. Single-particle strength and direct and semidirect decay cross sections

The optical-model potential for the proton relative to the ^{90}Zr core is needed to calculate the strength functions according to Eq. (4) and the direct and semidirect decay cross sections according to Eqs. (9) and (11). This potential was taken from Wang *et al.* [23] who made a dispersive optical-model analysis of proton scattering from ^{90}Zr . This potential has been used to reproduce the experimental single-proton

spectrum and the proton separation energy. Here, we use a modified version of this potential as suggested by Ref. [19].

The parameterization and parameters of the real and imaginary parts of the optical potential as functions of the proton energy ε_p are

$$U_{\text{opt}}(r, \varepsilon_p) = V_C(r) - V(r, \varepsilon_p) - iW_I(r, \varepsilon_p), \quad (16)$$

where $V_C(r)$ is the Coulomb potential of a uniformly charged sphere with a reduced radius $r_C = 1.264$ fm. The real part $V(r, \varepsilon_p)$, is given as

$$V(r, \varepsilon_p) = V_0(\varepsilon_p)f(r, r_0, a_0) + 2V_{\text{so}}\frac{1}{r}f'(r, r_{\text{so}}, a_{\text{so}})(\vec{l} \cdot \vec{s}). \quad (17)$$

The imaginary part $W_I(r, \varepsilon_p)$ is

$$W_I(r, \varepsilon_p) = W_W(\varepsilon_p)f(r, r_W, a_W) - 4a_D W_D(\varepsilon_p)f'(r, r_D, a_D). \quad (18)$$

The potentials are factorized as strength functions $V_0(\varepsilon_p)$, $W_W(\varepsilon_p)$, $W_D(\varepsilon_p)$, and V_{so} multiplied by a Woods-Saxon function f or its derivative $f' = \partial f / \partial r$, with

$$f(r, r_i, a_i) = (1 + \exp[(r - r_i)A^{1/3}/a_i])^{-1}. \quad (19)$$

The parameters V_0 , a_0 , and r_0 of the real potential for the proton bound to the ^{90}Zr core are listed in Table I and have been taken from Ref. [19]. For the spin-orbit part, V_{so} listed in Eq. (17), the parameters are $V_{\text{so}} = 5.9$ MeV fm², $r_{\text{so}} = 1.072$ fm, and $a_{\text{so}} = 0.63$ fm. The strength parameters of the imaginary part of the optical-model potential, W_i ($i = W, D$), are determined by

$$W_W(\varepsilon_p) = J_W(\varepsilon_p) / \left[\int f(r, r_W, a_W) d^3r \right], \quad (20)$$

$$W_D(\varepsilon_p) = -J_D(\varepsilon_p) / \left[\int 4a_D f'(r, r_D, a_D) d^3r \right]. \quad (21)$$

Here, the volume integrals $J_W(\varepsilon_p)$ and $J_D(\varepsilon_p)$ of the imaginary potential are approximated by the relations given in Refs. [23,24] as

$$J_i(\varepsilon_p) = \alpha_i \frac{(\varepsilon_p - \varepsilon_F)^4}{(\varepsilon_p - \varepsilon_F)^4 + \beta_i^4}, \quad i = (I, W), \quad (22)$$

$$J_D(\varepsilon_p) = J_I(\varepsilon_p) - J_W(\varepsilon_p) \quad (23)$$

TABLE I. Parameters of the real part of the proton optical potential (Woods-Saxon form; $a_0 = 0.68$ fm) as functions of the proton energy ε_p , taken from Ref. [19].

ε_p (MeV)	V_0 (MeV)	r_0 (fm)
1	54.735	1.280
5	53.246	1.290
10	51.589	1.277
15	50.157	1.258
20	48.931	1.240
25	47.870	1.224
30	46.912	1.210

TABLE II. Optical-model parameters used in the DWBA calculations.

Particle	V_0 (MeV)	r_0 (fm)	a_0 (fm)	W_W (MeV)	W_D (MeV)	r_I (fm)	a_I (fm)	V_{so} (MeV)	r_C (fm)	Ref.
α	118.4	1.24	0.79	21.7		1.54	0.59		1.3	[25]
t	131.4	1.218	0.677		20.6	1.128	0.939		1.3	[26]
p	varied	1.25	0.65					$\lambda = 25$	1.3	

with $\alpha_I = \alpha_W = 100$ MeV fm³, $\beta_I = 12.21$ MeV, $\beta_W = 60.3$ MeV, and $\varepsilon_F = -6.8$ MeV. The geometrical parameters depend on the energy range of ε_p . For $\varepsilon_p > 20$ MeV, the values are $r_W = r_D = 1.236$ fm and $a_W = a_D = 0.61$ fm. In the lower energy range, $\varepsilon_p < 20$ MeV, these parameters depend on ε_p , that is,

$$r_W(\varepsilon_p) = r_D(\varepsilon_p) = r_1 - r_2(\varepsilon_p - \varepsilon_F)^4 / [(\varepsilon_p - \varepsilon_F)^4 + \varepsilon_1^4], \quad (24)$$

$$a_W(\varepsilon_p) = a_D(\varepsilon_p) = a_1 + a_2(\varepsilon_p - \varepsilon_F)^4 / [(\varepsilon_p - \varepsilon_F)^4 + \varepsilon_2^4], \quad (25)$$

with $r_1 = 1.5$ fm, $r_2 = 0.276$ fm, $\varepsilon_1 = 12.3$ MeV, $a_1 = 0.18$ fm, $a_2 = 0.566$ fm, and $\varepsilon_2 = 20.1$ MeV.

For the calculation of the excitation cross sections for the different $\{l, j\}$ values, the strength function for a specific transition [see Eq. (4)] is folded with the DWBA cross sections. These DWBA cross sections $\sigma^{\text{DW}}(\theta, \varepsilon)$ are calculated using the code DWUCK [20]. For the α particle and tritons, the optical-model parameters, following the notation of Eqs. (16)–(18), were taken from Refs. [25] and [26], respectively; see Table II. The triton optical-model parameters are based on the ${}^3\text{He}$ optical-model parameters deduced from ${}^3\text{He}$ elastic scattering from ${}^{90}\text{Zr}$ at a bombarding energy of 89.3 MeV [27]. The parameters of the proton real optical-model potential are given in Table II. The proton s.p. wave function was determined by varying the potential depth to reproduce the proton binding or resonance energy. Furthermore, in the DWBA calculations for the ${}^{90}\text{Zr}(\alpha, tp)$, a finite-range correction parameter of 0.7 was used and the Vincent-Fortune procedure [28] for unbound levels was employed to calculate the DWBA cross sections.

Finally, the parameters β_L for ${}^{90}\text{Zr}$ which are used to describe the transition potentials according to Eq. (12) are taken from Ref. [29] and listed in Table III. The potential U used to describe the nuclear mean field for the protons needed in Eq. (12) is the part $V_0(\varepsilon_p)f(r, r_0, a_0)$ given by Eq. (17).

TABLE III. Dynamic deformation parameters β_L for the phonon states in ${}^{90}\text{Zr}$; from Ref. [29].

State	E_x (MeV)	β_L
2_1^+	2.18	0.07
3_1^-	4.16	0.20
5_1^-	4.56	0.08

2. Statistical-decay cross sections

The branching ratio $b_{ij,i}^{\text{stat}}$ for statistical decay of a s.p. state to a final state i , $b_i(E_x, lj)$, is calculated using the code CASCADE [3,30]. The cross sections for statistical decay are calculated by folding the spin distributions, following the procedure outlined in Sec. II B 1, with the calculated branching ratios $b_i(E_x, lj)$ related to them. For these calculations, the relevant parameters concerning the level densities for the various nuclei in the decay chain are listed in Table IV. For the lowest excitation-energy region, individual levels were used. These were taken from the literature [31] up to an excitation energy E_a , listed in Table IV, below which levels were well identified. In the excitation-energy region $E_a < E_x < E_b$, with $E_b \equiv 60A^{-1/3}$ MeV, the parameters of the back-shifted Fermi gas model from Dilg *et al.* [32] were used. In some cases, however, the value of Δ , the pairing energy that determines the zero point of the effective excitation energy, was adjusted slightly such that the sums of all levels determined in the different procedures match at the transition regions near E_a and E_b . Beyond an excitation energy $E_x = E_c \equiv 120A^{-1/3}$ MeV, the level densities are described by the liquid-drop model, with the level-density parameter $a = A/8$ MeV⁻¹. In the region $E_b < E_x < E_c$, the level-density parameters were calculated from extrapolations and interpolations of the level densities in the neighboring regions ($E_x < E_b$ and $E_x > E_c$).

III. EXPERIMENTAL PROCEDURE AND RESULTS

A. The experimental setup

The ${}^{90}\text{Zr}(\alpha, tp)$ experiment was performed at the Research Center for Nuclear Physics (RCNP), Osaka University using 180 MeV α -particles from the RCNP ring cyclotron. The tritons were analyzed using the Grand Raiden spectrometer [33]. The horizontal acceptance of the spectrometer was 40 mrad, which is the maximum in the bending plane; slits were used for the vertical acceptance, allowing an acceptance of also

TABLE IV. Parameters used in the statistical-model calculations.

Nucleus	a (MeV ⁻¹)	Δ (MeV)	E_a (MeV)
${}^{91}\text{Nb}$	9.0	-0.20	2.034
${}^{90}\text{Nb}$	9.0	-1.40	0.813
${}^{90}\text{Zr}$	9.0	1.86	4.126
${}^{89}\text{Zr}$	9.0	0.21	2.995
${}^{89}\text{Y}$	9.0	0.90	3.138

40 mrad. Therefore, the solid angle during the experiment was 1.6 msr. The direct beam from the cyclotron was stopped in a well-shielded Faraday cup, from which the current was measured and integrated. For ^{90}Zr we used a 1 mg/cm² thick metallic target, isotopically enriched to 98%. For calibration purposes we used a 2 mg/cm² thick ^{90}Zr target and a natural carbon target with a thickness of 4 mg/cm².

Although the cross sections for the population of high-spin states are maximum at 0°, the spectrometer was positioned at a scattering angle of 0.3°. This was done because it was found that in the focal-plane detector system the background from the Faraday cup is the lowest at the angle at which the direct beam is stopped somewhat more upstream from its nominal position at 0°. The magnetic fields of the spectrometer were set such that excitation energies in ^{91}Nb between 6 and 21 MeV were covered. Additional (singles) measurements were done with magnet settings at which lower excitation energies, including the g.s. of ^{91}Nb , were also observed. Furthermore, measurements were made using a carbon target. The combination of these data and those of the low excitation-energy region was used for the energy calibration of the detected tritons in the focal-plane detectors. These detectors were a set of two multiwire-drift chambers (MWDC's) backed by two plastic scintillator arrays [34]. Each MWDC has x , u , and v planes for the determination of the trajectory of a detected particle at the position of the focal plane. Between the two scintillators, a 1 cm thick aluminum plate was placed which is thin enough to allow tritons to pass through. Heavier ions, such as α particles, were stopped in this plate. Therefore, the second scintillator was used as a coincidence detector for tritons, substantially reducing the singles count rate and possible sources of background. The energy resolution obtained for the tritons detected in the focal-plane detector was 150 keV (full width at half maximum, FWHM), mainly determined by the spread of the energy in the incoming beam.

Protons emitted from the excited ^{91}Nb nuclei were detected using a setup consisting of 37 lithium-drifted silicon solid-state detectors (SSD's). These detectors, with a thickness of 5 mm and an area of 400 mm² each, were mounted in a spherical structure at a distance of 10 cm from the target, covering backward angles between 100° and 160°. To reduce possible edge effects in these detectors, their acceptance was limited with a 21 mm diameter diaphragm. The solid angle per detector was 15.4 msr. The number of detectors and the total solid angle at each polar angle are listed in Table V. The energy calibration

of the silicon detectors was done using 5.486 MeV α particles from a ^{241}Am source. In addition, coincidence data for the $^{12}\text{C}(\alpha, tp)$ reaction were measured and used to calibrate the proton detectors. After proton decay from an excited state in ^{91}Nb , the energy of the final state in ^{90}Zr is given by

$$E_{\text{final}} = E_x(^{91}\text{Nb}) - E_p - S_p - E_r, \quad (26)$$

where E_r is the recoil energy of the ^{90}Zr nucleus. The energy resolution obtained for the final-state spectra was 300 keV (FWHM).

The complete setup (except for the number of SSD's) and data-acquisition system used in this experiment were very similar to the ones used by Akimune *et al.* [35]. Both singles and coincidence events were recorded event by event, and scalers were used to record the integrated beam current and the dead time of the data-acquisition system. These were read out at regular intervals. For the protons, both the energy signal and the timing signal with respect to that from the focal-plane detector were recorded. Two coincidence windows were set to record prompt and random coincidence events. The trigger for the first window was set to record protons originating from the beam burst related to prompt tritons. The second window instead recorded protons arriving after or before the burst associated with prompt tritons. In this way, both prompt and random coincidences were recorded, and in the off-line analysis the prompt events were corrected for random contributions.

To obtain an overall normalization of the cross sections, singles measurements were made for the population of the IAS's in the range between 0° and 8° in steps of 2°. Since the spectroscopic factor for the transition to the g.s. of ^{91}Nb is well known [36,37], the cross section for this transition near 0° was also used for the normalization of the absolute cross sections. For this purpose, a singles measurement was also performed at KVI with the Big-Bite magnetic spectrometer (BBS) [38]. The BBS was set at 4° with horizontal and vertical opening angles of 4° and 6°, respectively. A 180 MeV α -particle beam from the AGOR (Accélérateur Groningen-ORsay) cyclotron bombarded a 5 mg/cm² ^{90}Zr target. The triton ejectiles were detected with the EuroSuperNova (ESN) detector [39,40]. This allowed the identification of the particles through their energy loss in two scintillator pads and their time of flight through the BBS. Two vertical-drift chambers furnished information on the x and y positions of the tritons at the focal plane. This further allowed us to determine the momenta and the horizontal and vertical angles of incidence at the focal plane. The scattering angle could then be reconstructed with ray-tracing algorithms. The deduced differential cross sections for the population of the $J^\pi = 9/2^+$ g.s. and the $J^\pi = 11/2^-$ IAS at $E_x = 12$ MeV in ^{91}Nb are shown as dots in Fig. 1. The systematic error in the absolute cross sections is taken to be 20%. The data for the IAS obtained earlier at RCNP are also shown in Fig. 1 (open circles). They were normalized to the more recent KVI data. A renormalization factor of 3.0 was needed. All cross sections presented in Refs. [12] and [13] should be multiplied by this factor.

TABLE V. Number of proton detectors at different polar angles.

θ_p (lab.)(deg)	Number of detectors	$\Delta\Omega_{\text{total}}$ (msr)
160	4	61.6
150	5	77.0
140	6	92.4
130	5	77.0
120	6	92.4
110	5	77.0
100	6	92.4

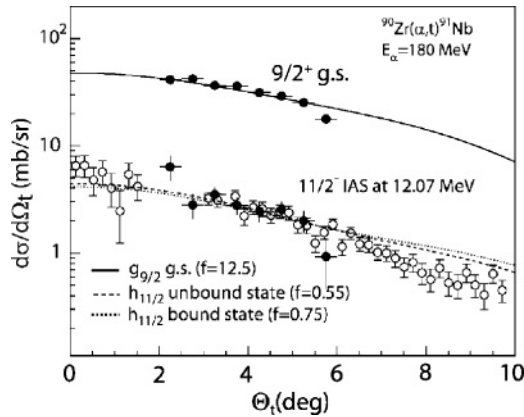


FIG. 1. Differential cross sections (filled circles) for the population of the ground state and the IAS at $E_x = 12.07$ MeV in ^{91}Nb obtained from a measurement at KVI. The more extensive data for the IAS (open circles) were obtained at RCNP. Curves are the results of DWBA calculations assuming a $g_{9/2}$ transfer for the g.s. transition and an $h_{11/2}$ transfer for the IAS transition. The two curves for the IAS are obtained with an unbound s.p. wave function employing the Vincent-Fortune procedure for the DWBA calculation (dashed curve) and a slightly bound wave function (dotted curve); see text for more details. Normalization factors f are obtained by normalizing σ_{ij}^{DW} to the data.

B. Data reduction

As a first step in the analysis, the position and angle of the particles crossing the focal plane were calculated from the data of the MWDC's. A good reconstruction of the scattering angle in the vertical plane was not possible because of the large magnification of the spectrometer in the vertical direction, $M_y = 6.0$. Background, most likely coming from the Faraday cup, appeared to be present in the excitation-energy spectra. This background could be removed successfully using a gate on the triton time-of-flight data. In the proton-energy spectra, background was observed at low (mainly below 2 MeV) proton energy. To remove this background, a gate was applied to the two-dimensional spectra of proton energy versus the arrival time difference between the proton and triton detection signals.

C. Calibration data

In the off-line analysis, the $^{12}\text{C}(\alpha, t)$ data were analyzed for consistency checks [41]. Figure 2 displays the kinetic energy of protons emitted from the excited nuclei versus the excitation energy in ^{13}N . The decay to the g.s. of ^{12}C and to its first excited state at $E_x = 4.44$ MeV can be seen as the two loci with constant values for $E_x - E_p$. In addition, a locus from the $^{16}\text{O}(\alpha, tp_0)$ can be seen in this plot. This locus stems from a contamination of the carbon target with oxygen. Using the level schemes for ^{13}N [42] and ^{17}F [43], strong peaks in these nuclei could be identified and were used as calibration points for the analysis of the $^{90}\text{Zr}(\alpha, t)$ data. The levels concerned are those at $E_x = 3.55, 6.36,$ and 10.36 MeV in ^{13}N and the one at $E_x = 5.82$ MeV in ^{17}F .

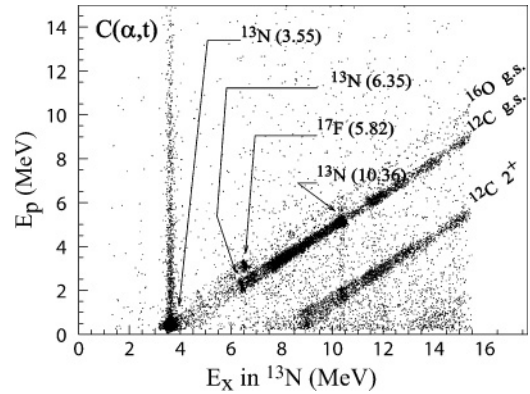


FIG. 2. Two-dimensional scatter plot of the energy of detected protons E_p vs the excitation energy E_x in ^{13}N for the $^{12}\text{C}(\alpha, t)$ reaction used as a calibration during the experiment. Labeled loci correspond to different final states (g.s. and 2^+ state at $E_x = 4.4$ MeV) in ^{12}C or to the g.s. of ^{16}O from contaminants.

D. Singles (α, t) data

Figure 3 shows the measured singles $^{90}\text{Zr}(\alpha, t)$ spectrum. This spectrum was made by combining two independent singles spectra measured at two different settings of the magnetic fields of the spectrometer, one covering the lower excitation energy, the other one the region that was used during the decay study. The difference in statistics for the two different settings explains the strong fluctuations seen in the lower excitation-energy region. In this region, the g.s. and low-lying states in ^{91}Nb are observed as narrow peaks. For instance, it is easy to identify the peaks at $E_x = 3.43$ and 4.82 MeV [44] in ^{91}Nb , which are also strongly excited in the $^{90}\text{Zr}(^3\text{He}, d)$ reaction [36]. Above 6 MeV excitation energy, broader structures are observed on top of a continuum which is rising with energy. The dominant narrow peak at ~ 12 MeV was identified as an IAS (see Refs. [13,45,46]). Two peaks caused by contamination of the target are labeled $^{13}\text{N}(3.55)$ and $^{17}\text{F}(5.82)$; they are due to the $^{12}\text{C}(\alpha, t)$ and $^{16}\text{O}(\alpha, t)$ reactions leading to final states at $E_x = 3.55$ and 5.82 MeV in ^{13}N and ^{17}F , respectively.

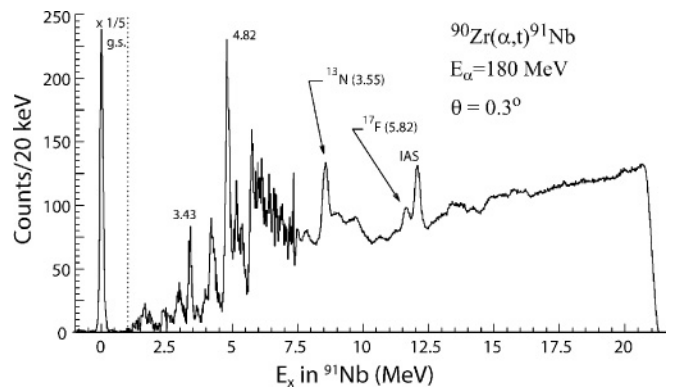


FIG. 3. Singles spectrum for the $^{90}\text{Zr}(\alpha, t)$ reaction measured at $\theta = 0.3^\circ$. Two magnetic-field settings of the spectrometer were used. Region below 7.5 MeV was normalized to the high-energy region. In addition, an IAS of ^{91}Nb and known states due to the contaminants ^{12}C and ^{16}O are indicated.

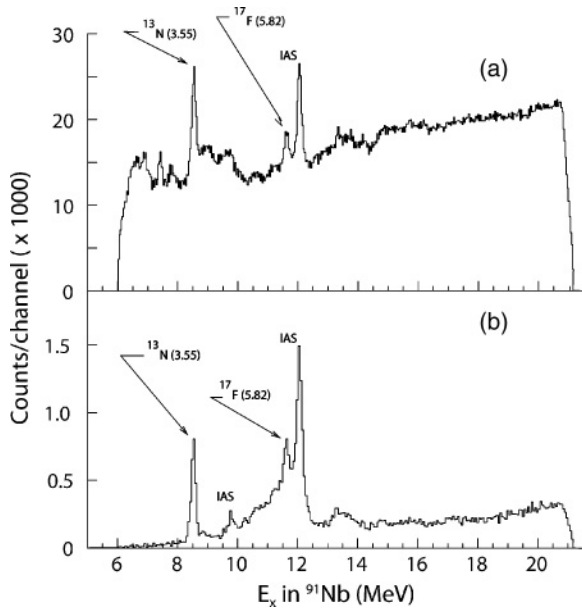


FIG. 4. Comparison between the singles spectrum (a) and the spectrum for which a coincidence with a proton emitted at backward angles is required (b). See also the caption of Fig. 3.

E. Coincidence (α , tp) data

In Fig. 4, the inclusive excitation-energy spectrum is compared with the spectrum from the coincidence data, i.e., tritons detected in the focal plane simultaneously with a proton detected in a SSD. The coincidence spectrum rises from 6 to 12 MeV because of the opening of the proton channel ($S_p = 5.15$ MeV). Above the neutron-emission threshold, $S_n = 12.05$ MeV, neutron decay is possible, and the decay by protons is reduced. A striking observation is the strong reduction of the continuum background in the coincidence spectrum compared to that in the singles spectrum. Most likely, this continuum background is caused by breakup of α particles into a triton and a proton. In this process, these two particles are emitted mainly in the forward direction. Thus, requiring a coincidence with a proton emitted at backward angles strongly reduces the contribution of this process. In the two-dimensional spectrum of the proton energy versus the excitation energy in ^{91}Nb (see Fig. 5), some final states in ^{90}Zr can be clearly identified as loci with a constant value for $E_x - E_p$. Also indicated are the loci for the decay of ^{13}N and ^{17}F to the g.s.'s of ^{12}C and ^{16}O , respectively.

In Fig. 6, the excitation-energy spectra are shown for three different gates on the final-state energy. In Fig. 6(a), this spectrum is shown for coincidence events leading to the population of the g.s. of ^{90}Zr . In this case, events caused by target contaminants of either ^{16}O or ^{12}C are not present because kinematically their loci are well separated from the locus for decay to the g.s. of ^{90}Zr . In Fig. 6(b), the excitation-energy spectrum for the decay to the $2^+_1/5^-_1$ doublet is shown. The energy resolution in the present experiment was not good enough to separate these two peaks in the final-state spectrum, which are located at $E_x = 2.19$ and 2.32 MeV in ^{90}Zr , respectively. Figure 6(c) displays the excitation-energy spectrum using a coincidence gate for the population of the

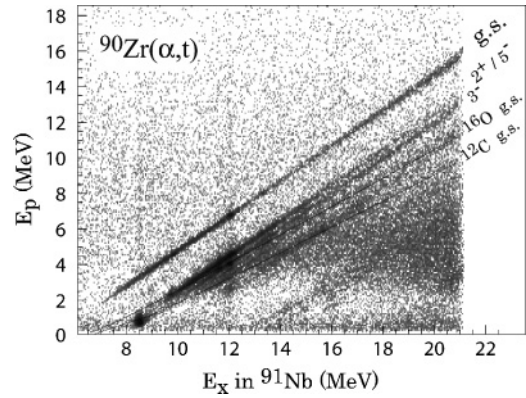


FIG. 5. Two-dimensional scatter plot of the energy of detected protons E_p vs the excitation energy E_x in ^{91}Nb . Labeled loci correspond to different final states in ^{90}Zr or to the g.s.'s of ^{12}C and ^{16}O . Solid lines are the calculated loci for the (α , tp) reaction on the oxygen and carbon contaminants.

3^-_1 state in ^{90}Zr , which is located at an excitation energy of 2.75 MeV. Because of the opening of the neutron-decay channel at an excitation energy of 12.05 MeV in ^{91}Nb , the data for the 6–12 MeV excitation-energy range and for the range beyond 12 MeV will be discussed separately.

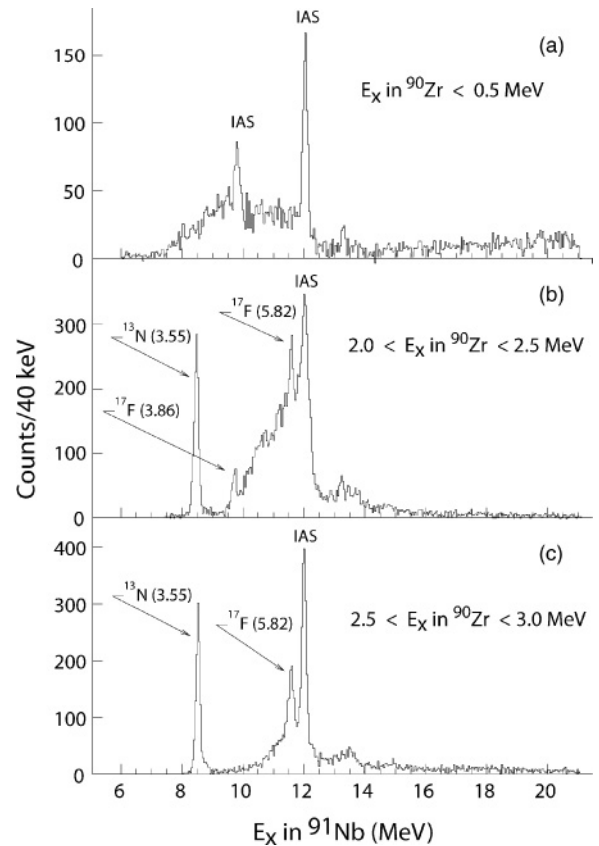


FIG. 6. Spectra for tritons in coincidence with protons leading to the population of different states in ^{90}Zr : to the g.s. (a), to the $2^+_1/5^-_1$ doublet (b), and to the 3^-_1 state (c). See also the caption of Fig. 3.

1. Decay from levels below the neutron-emission threshold

In the excitation-energy region below 12.05 MeV, decay of excited states is only possible through proton or γ -ray emission. As can be seen from Fig. 6, below 10.0 MeV in excitation energy in ^{91}Nb , almost no proton decay occurs to states other than the g.s. of ^{90}Zr . Although energetically allowed, the decay from states in the region just above the threshold for proton emission is suppressed because of the Coulomb and centrifugal barriers. This is also the reason that decay to the low-lying phonon states in ^{90}Zr is only observed for excitation energies above 9 MeV in ^{91}Nb . In the region between the two IAS's [see Fig. 6(a)], decay is observed to the g.s., the $2_1^+/5_1^-$ doublet, and the 3_1^- state.

2. Decay from levels above the neutron-emission threshold

The final-state spectra for different excitation-energy regions in ^{91}Nb are shown in Fig. 7. Decay is observed to the g.s. of ^{90}Zr , low-lying phonon states, and higher-lying states which are not resolved. The rather large amount of decay to the g.s. is striking, especially from high excitation energies. Furthermore, the decay to the g.s. of the contaminants ^{12}C and ^{16}O and to the first excited state of ^{12}C is seen. In Figs. 7(b) and 7(c), the final-state spectrum from the $^{12}\text{C}(\alpha, tp)$ reaction, using the kinematics of the $^{90}\text{Zr}(\alpha, tp)$ reaction, is also shown as a dotted histogram.

IV. DISCUSSION

A. Calculated single-particle strength

The strength functions for the different $\{l, j\}$ values were calculated using the approach described in Secs. II A1 and II B1. The results of these calculations are shown in Fig. 8. From the measured differential cross sections and the DWBA calculations made with the code DWUCK [20], we determined the overall normalization factor N needed in Eq. (1). The results of the DWBA calculations for the transitions to the g.s. and to the IAS at $E_x = 12.07$ MeV are compared with the data in Fig. 1. The factors f that normalize the DWBA calculations to the data, σ^{DW} , are given in the figure. The $g_{9/2}$ spectroscopic factor for the ^{91}Nb g.s. is known to be $C^2S = 0.87$ [36,37]. Making use of Eq. (2), this yields a normalization factor $N = 14.4$. Considering the large systematic uncertainty of 20% in the absolute cross sections, the deduced normalization factor of $N = 14.4$ agrees with the value of 18.2 published by Das *et al.* [47], based on the systematics for the (α, t) reaction. With this normalization factor, the spectroscopic factor for the $11/2^-$ IAS at 12.07 MeV is deduced to be 0.038 assuming an unbound wave function derived at the exact resonance energy and employing the Vincent-Fortune procedure. On the other hand, a spectroscopic factor of 0.052 was derived assuming a wave function that is slightly bound by about 150 keV. These values are in good agreement with the experimental spectroscopic factor of the $11/2^-$ parent state in ^{91}Zr of $S_v(1h_{11/2}) = 0.37$ [48] and $S_v(1h_{11/2}) = 0.45$ [49]. Note that these values should be multiplied by the isospin Clebsch-Gordan coefficient, $C^2 = 1/11$, yielding 0.034 and 0.041,

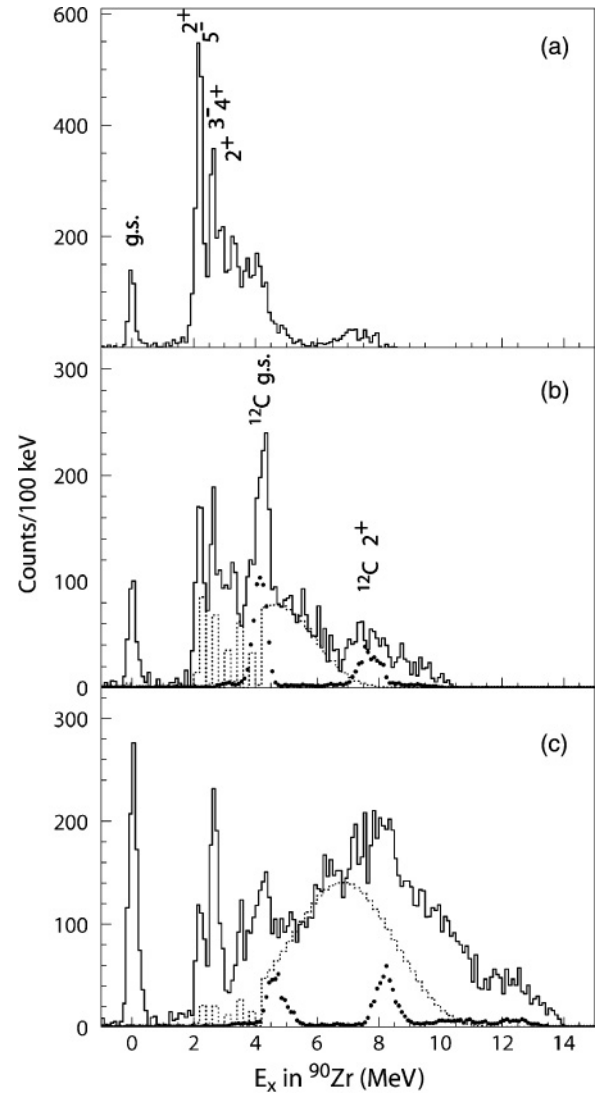


FIG. 7. Final-state spectra for decay from the excitation-energy regions in ^{91}Nb of 12.2–14.0 MeV (a), 14.0–16.0 MeV (b), and 16.0–20.0 MeV (c). Also shown are the measured final-state spectrum from the $^{12}\text{C}(\alpha, tp)$ reaction (Ref. [41]; dots) and the normalized statistical-model calculations (dashed histograms). Extra strength observed in (c) could likely be due to contributions from the $^{16}\text{O}(\alpha, tp)$ reaction.

respectively, before comparing them with the spectroscopic factors of the IAS.

The strength functions shown in Fig. 8, calculated following the procedure described in Sec. II A1, were folded with the DWBA cross sections σ_{ij}^{DW} for the different values of $\{l, j\}$; see Fig. 9. These do not include the factor $NC^2S = 14.4 \times 10/11$ necessary to compare with experimental cross sections. It is seen in Fig. 9 that although we only cover the tail of the strength function of the $i_{13/2}$ state, this state accounts for a large fraction of the cross section at higher excitation energy. This is a result of the selectivity for the population of high-spin states in this reaction. Because the uncertainty (up to 50%) in the strength functions is rather large in the tails of these functions [50], the resulting calculated cross sections have

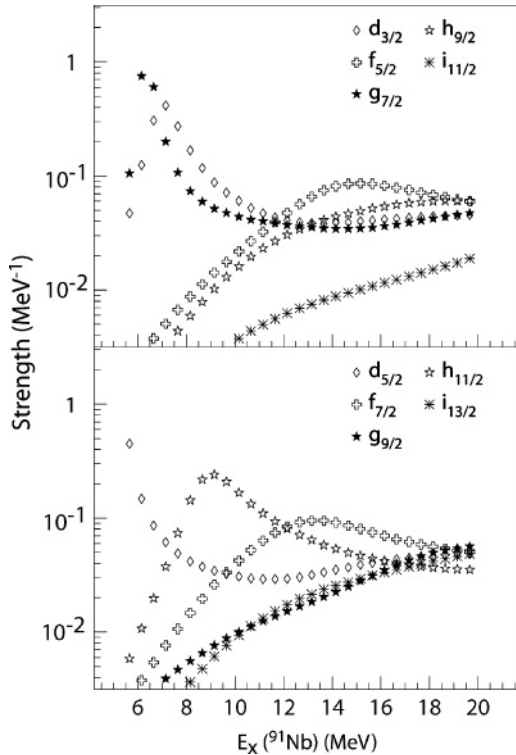


FIG. 8. Calculated s.p. strength functions as a function of the excitation energy in ^{91}Nb for different s.p. states.

also a similar uncertainty. Also shown in Fig. 9 is the sum of all calculated contributions. The spectrum is dominated by two broad structures at about 6 and 9 MeV related to $g_{7/2}$ and $h_{11/2}$ states, respectively. In an experiment performed with the one-proton stripping reaction $^{90}\text{Zr}(^7\text{Li}, ^6\text{He})$, similar broad states were observed at the same excitation energies [9]. The presence of a large background and contaminant states makes a more quantitative comparison between the present data and those of the $(^7\text{Li}, ^6\text{He})$ reaction impossible. At higher excitation energies, more overlapping broad states contribute to the yield where the main contributions are from the high-spin $i_{13/2}$, $h_{11/2}$, and $h_{9/2}$ states.

B. Decay cross sections

The angular correlation of the decay from the excitation energies below the neutron-emission threshold in ^{91}Nb (see Sec. III E 1) to the g.s. can be described very well by assuming $h_{11/2}$ strength for this region; see Fig. 10. Also from Fig. 6, it can be seen that the proton is emitted from a high-spin state. This is because as soon as it is energetically allowed, decay to the 5_1^- state and to a lesser extent to the 3_1^- state become the dominant decay channels. Decay to the g.s. is hindered by the angular-momentum barrier. The cross section in this region for decays to the different final states in ^{90}Zr is calculated by integrating the theoretical cross sections. These have been fitted over all proton angles to the measured angular correlation functions. This is done using excitation-energy intervals with a width of 0.5 MeV. The results are shown in Fig. 11. The theoretical strength distribution shown in Fig. 9 is dominated

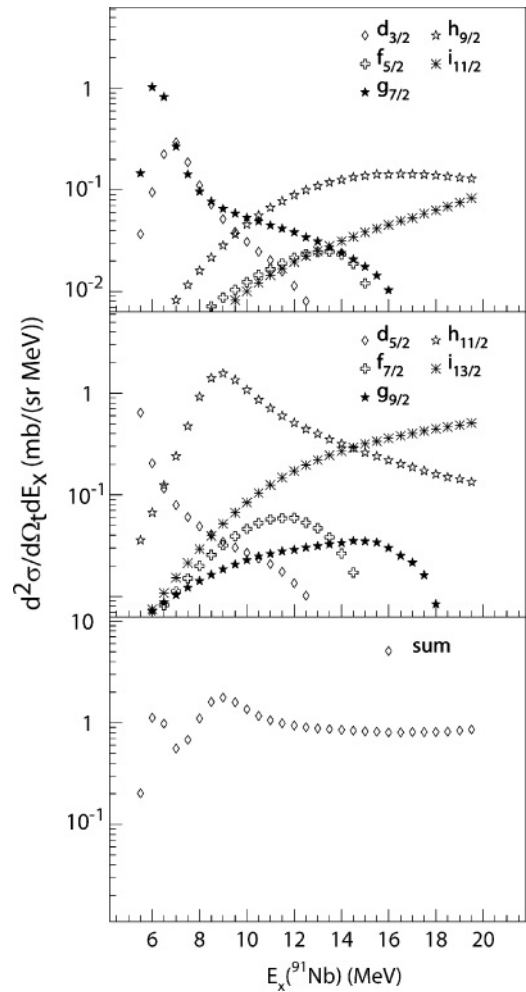


FIG. 9. Double-differential cross sections of $^{90}\text{Zr}(\alpha, t)$ reaction at $E_\alpha = 180$ MeV, obtained by folding calculated s.p. strength functions with σ^{DW} (i.e., not including the factor NC^2S) at $\theta_t = 0^\circ$ as a function of the excitation energy in ^{91}Nb , are shown in the upper and middle parts of the figure. In the lower part, the summed yield ($d_{3/2}$ to $i_{13/2}$) is shown.

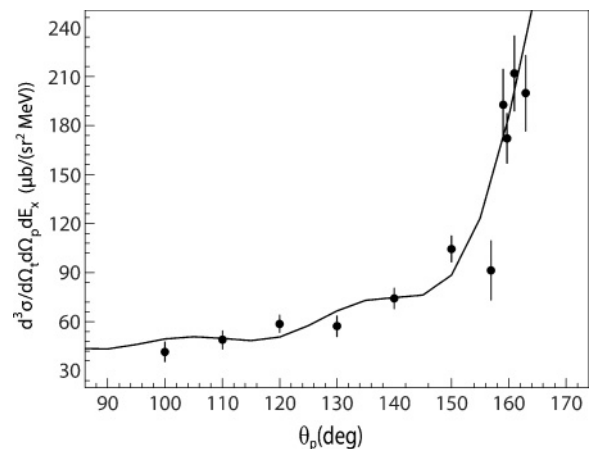


FIG. 10. Experimental angular correlations (dots) compared to a calculation assuming $h_{11/2}$ for the decay from the 10.0–11.5 MeV excitation-energy region in ^{91}Nb leading to the g.s. in ^{90}Zr [see Fig. 6(a)].

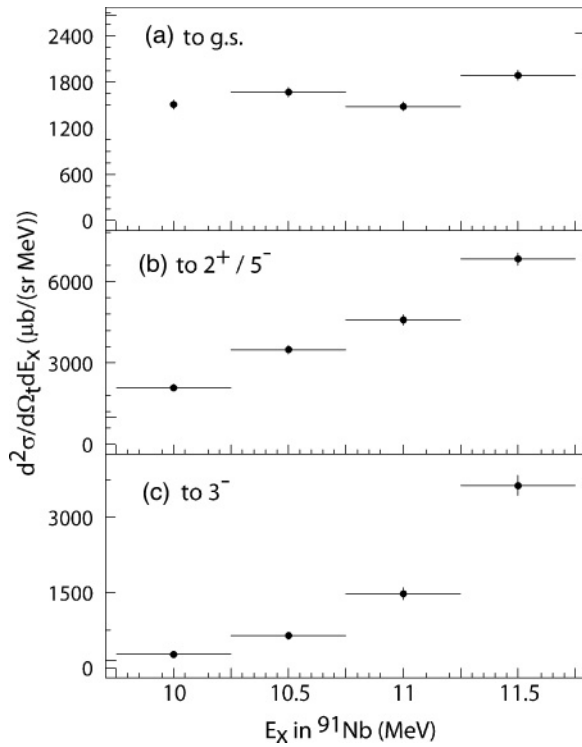


FIG. 11. Double-differential cross sections obtained after integration over the proton angle for decay from the excitation-energy bin between 10.0 and 11.5 MeV in ^{91}Nb to the g.s. (a), to the $2_1^+/5_1^-$ doublet (b), and to the 3_1^- state (c) in ^{90}Zr .

by the $h_{11/2}$ state in this energy range, which explains the dominance of the ($l = 0$) transition to the 5^- state. The high spin of the states excited in this region is confirmed by the observed angular correlation of the emitted proton for decay to the g.s. of ^{90}Zr .

Also for the region in ^{91}Nb above the neutron-emission threshold (see Sec. III E2), cross sections related to the decay to different final states were obtained by an integration over the proton angle. For this procedure, theoretical angular correlations were fitted to the experimental correlations; see Sec. II A4. For the region $E_x(^{91}\text{Nb}) = 12\text{--}15$ MeV, the main contribution is the $h_{11/2}$ state with small contributions from several other states. The relative contributions are dependent on $E_x(^{91}\text{Nb})$. The calculated angular correlation does not reproduce the experimental correlation if one assumes a small contribution from the $i_{13/2}$ state. In Fig. 6(a), a small sharp peak is seen at 13 MeV. This peak corresponds possibly to another IAS. This peak is excluded by using only the excitation-energy range 13.5–15.0 MeV in ^{91}Nb . A satisfactory description of the experimental correlation is obtained if we assume that the excitation strength in this region is due to an $h_{11/2}$ state with a small contribution of an $i_{13/2}$ state [see Fig. 12(a)]. The obtained cross sections, integrated over the proton solid angle, for decay to the g.s. and to low-lying states are shown in Fig. 13. For the decay to the g.s. from the region $E_x(^{91}\text{Nb}) = 15\text{--}20$ MeV, the angular correlation was calculated using an $i_{13/2}$ state with admixture of an $h_{11/2}$ state where the (average) ratio of the calculated cross sections for the two states was

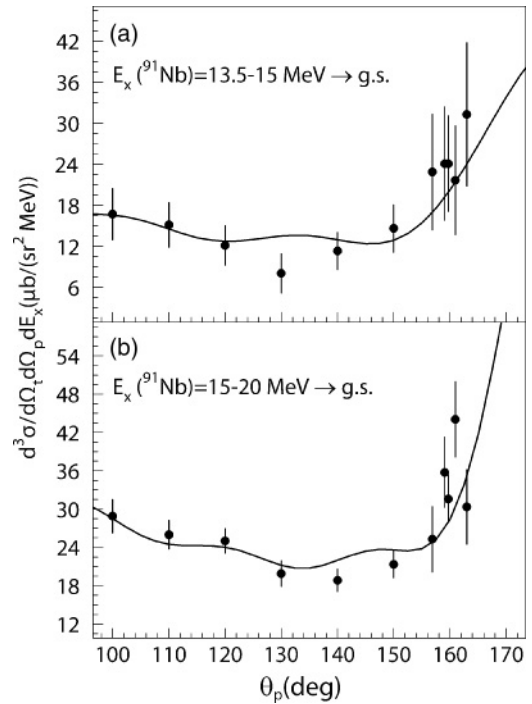


FIG. 12. Calculated (solid lines) and experimental (dots) angular correlations for the decay from states in ^{91}Nb to the g.s. of ^{90}Zr from the regions $E_x(^{91}\text{Nb}) = 13.5\text{--}15.0$ MeV (a) and $15.0\text{--}20.0$ MeV (b); see text for more details.

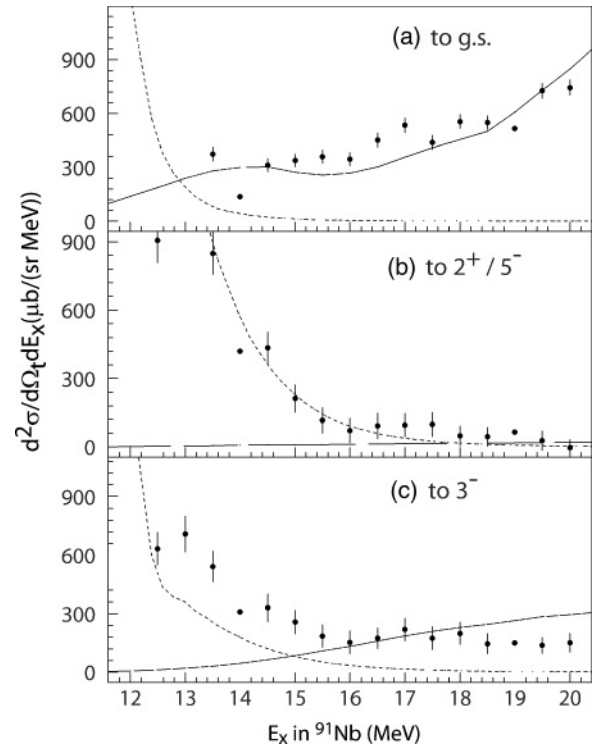


FIG. 13. Double-differential cross sections obtained after integration over the proton angle, for decay to the g.s. (a), to the $2^+/5^-$ states (b), and to the 3^- state (c) as a function of $E_x(^{91}\text{Nb})$. Also shown are the calculated cross sections for direct and semidirect decay (solid lines) and statistical decay (dashed lines).

used; see Fig. 9. The obtained correlation function describes the experimental data very well as is shown in Fig. 12(b).

1. Statistical decay

The statistical-decay cross sections are calculated as described in Sec. II B2 and normalized to the experimental decay cross sections, assuming that the decay to higher-lying states is completely statistical. This decay is observed as broad peaks in the final-state spectrum. This is shown in Fig. 7, where broad peaks can be seen between 4 and 6 MeV [Fig. 7(b)] and between 4 and 10 MeV [Fig. 7(c)]. It is seen in Fig. 7(c) that above 8 MeV the measured strength cannot be explained by statistical-model calculations and the ^{12}C spectrum. It is likely that the extra strength is due to the $^{16}\text{O}(\alpha, tp)$ reaction, where excited states in ^{16}O are populated.

2. Direct decay

The direct decay from a state $\{l, j\}$ in ^{91}Nb to the different final states in ^{90}Zr through a transition L^π is calculated by folding the calculated excitation cross section shown in Fig. 9 with the branching ratio $b_{lj, L^\pi}^{\text{D,SD}}$ described in Sec. II and multiplying by the factor NC^2S . Double-differential cross sections obtained from the present experiment are shown in Fig. 13. In addition, the cross sections calculated for direct and semidirect decays to the different final states are displayed, summed over all relevant states $\{l, j\}$ in ^{91}Nb . Furthermore, the cross sections calculated for statistical decay are also shown. At excitation energies just above the neutron-emission threshold, the spectra are dominated by statistical decay and at higher energies by direct decay. Up to the highest excitation energy in ^{91}Nb , a considerable amount of decay to the g.s. is observed. Because no significant statistical decay to the g.s. is predicted by the statistical-model calculations, the decay to the g.s. can be attributed to direct decay. Fast processes like breakup of the α particle in a triton and a proton cannot explain the observed population of the g.s. of ^{90}Zr . Protons in this process are emitted predominantly in forward directions, whereas the observed angular correlation for the decay to the g.s. clearly shows an increase at far backward angles; see Fig. 12. The experimentally observed cross sections can be described well with the calculated direct and semidirect decay. For the decay to the $2_1^+/5_1^-$ doublet, statistical decay plays an important role. In the region below 16 MeV, the total experimental cross section can be described with the calculated statistical-decay cross section. For the 3_1^- state, more decay is experimentally observed than is calculated in the statistical model. For excitation energies $E_x > 15$ MeV in ^{91}Nb , the direct and semidirect decays dominate the decay to the g.s. and to the low-lying phonon states, respectively. This difference

between the experimentally observed cross sections and the statistical-decay calculations can be explained reasonably well by the calculations. A significantly stronger decay to the 3_1^- state compared with the $2_1^+/5_1^-$ doublet is seen both in the calculations and the experimental spectra, reflecting the strong coupling to the 3^- phonon state which was also observed in neutron-decay experiments [11].

V. SUMMARY AND CONCLUSION

The excitation and decay by proton emission of high-lying high-spin states in ^{91}Nb have been studied. Broad states have been observed at $E_x \sim 6$ and 9 MeV, consistent with results from calculations which predict the $g_{7/2}$ and $h_{11/2}$ states at these energies. At higher excitation energies, several overlapping high-spin states contribute to the cross section. Decay from these states by proton emission was seen to the low-lying phonon states, especially to the 3^- phonon state. This confirms the conclusions from other experiments that these states play an important role in the first steps of the damping mechanism of high-lying high-spin s.p. states. Even at high excitation energies, proton decay to the g.s. has been clearly observed. The angular correlations corresponding to this decay show that a significant part of this decay must be attributed to direct decay. The measured decay cross sections to the g.s. and low-lying phonon states are very well described by calculations using an optical-model coupled-channel approach.

In conclusion, the study of proton decay of high-lying s.p. states has shown to be a powerful tool in the investigation of the damping mechanisms of such states. One can benefit from the good energy resolution and high efficiency for the detection of the protons, even at high proton energies. Furthermore, the results are much less dependent on the statistical-model calculations than are the results of neutron-decay experiments because of the strong reduction of the statistical decay by protons once the neutron channel opens.

ACKNOWLEDGMENTS

The authors wish to thank the cyclotron crew and the technical staff from RCNP and KVI for their support. This work was performed as part of the research program of the Stichting voor Fundamenteel Onderzoek der Materie (FOM) with financial support from the Nederlandse Organisatie voor Wetenschappelijk Onderzoek (NWO). The authors (V.A.R. and M.H.U.) acknowledge the support from NWO for their stay at the KVI. The authors (A.M.v.d.B., M.N.H., N.K.-N. and H.K.T.v.d.M.) acknowledge the support from the Japanese Ministry of Education (Monbusho) during their stay in Japan. J.J. and T.W.O'D. were supported in part by the U.S.-Japan Cooperative Research Program.

- [1] S. Galès, Ch. Stoyanov, and A. I. Vdovin, Phys. Rep. **166**, 125 (1988).
 [2] Nguyen Van Giai and Ch. Stoyanov, Phys. Lett. **B272**, 178 (1991).

- [3] F. Pühlhofer, Nucl. Phys. **A280**, 267 (1977).
 [4] M. N. Harakeh, A. van der Woude, J. van Popta, S. Y. van der Werf, and R. H. Siemssen, KVI Annual Report, 1975 (unpublished), p. 22.

- [5] S. Galès, C. P. Massolo, S. Fortier, J. P. Schapira, P. Martin, and V. Comparat, *Phys. Rev. C* **31**, 94 (1985).
- [6] C. P. Massolo, F. Azaiez, S. Galès, S. Fortier, E. Gerlic, J. Guillot, E. Hourani, and J. M. Maison, *Phys. Rev. C* **34**, 1256 (1986); C. P. Massolo, S. Fortier, S. Galès, F. Azaiez, E. Gerlic, J. Guillot, E. Hourani, H. Langevin-Joliot, J. M. Maison, J. P. Schapira, and G. M. Crawley, *Phys. Rev. C* **43**, 1687 (1991).
- [7] S. Fortier, S. Galès, S. M. Austin, W. Benenson, G. M. Crawley, C. Djalali, J. S. Winfield, and G. Yoo, *Phys. Rev. C* **41**, 2689 (1990).
- [8] G. H. Yoo, G. M. Crawley, N. A. Orr, J. S. Winfield, J. E. Finck, S. Galès, Ph. Chomaz, I. Lhenry, and T. Suomijärvi, *Phys. Rev. C* **47**, 1200 (1993).
- [9] S. Galès, *Nucl. Phys. A* **569**, 393c (1994).
- [10] D. Beaumel, S. Fortier, S. Galès, J. Guillot, H. Langevin-Joliot, H. Laurent, J. M. Maison, J. Veronotte, J. A. Bordewijk, S. Brandenburg, A. Krasznahorkay, G. M. Crawley, C. P. Massolo, and M. Rentería, *Phys. Rev. C* **49**, 2444 (1994).
- [11] S. Fortier, D. Beaumel, S. Galès, J. Guillot, H. Langevin-Joliot, H. Laurent, J. M. Maison, J. Bordewijk, S. Brandenburg, A. Krasznahorkay, G. M. Crawley, C. P. Massolo, M. Rentería, and A. Khendriche, *Phys. Rev. C* **52**, 2401 (1995).
- [12] H. K. T. van der Molen, Ph.D. thesis, University of Groningen, 1999.
- [13] H. K. T. van der Molen, H. Akimune, A. M. van den Berg, I. Daito, H. Fujimura, Y. Fujita, M. Fujiwara, M. N. Harakeh, F. Ihara, T. Inomata, K. Ishibashi, J. Jänecke, N. Kalantar-Nayestanaki, H. Laurent, I. Lhenry, T. W. O'Donnell, V. A. Rodin, A. Tamii, H. Toyokawa, M. H. Urin, H. Yoshida, and M. Yosoi, *Phys. Lett. B* **502**, 1 (2001).
- [14] T. Tamura, *Rev. Mod. Phys.* **37**, 679 (1965).
- [15] V. V. Samoilov and M. H. Urin, *Nucl. Phys. A* **567**, 237 (1994).
- [16] G. A. Chekomazov and M. H. Urin, *Phys. Lett. B* **349**, 400 (1995).
- [17] M. H. Urin and G. A. Chekomazov, *Phys. At. Nucl.* **61**, 375 (1998).
- [18] N. Van Giai, Ch. Stoyanov, V. V. Voronov, and S. Fortier, *Phys. Rev. C* **53**, 730 (1996).
- [19] E. A. Romanovsky, O. V. Bepalova, S. A. Goncharov, D. V. Pleshkov, and T. I. Spasskaya, *Phys. At. Nucl.* **63**, 399 (2000).
- [20] P. D. Kunz, computer code DWUCK, University of Colorado (unpublished); J. R. Comfort and M. N. Harakeh, extended versions of DWUCK.
- [21] M. H. Urin, *Sov. J. Part. Nucl.* **8**, 331 (1977).
- [22] M. N. Harakeh and L. W. Put, computer code ANGOR, KVI Internal Report KVI-67, 1981 (unpublished).
- [23] Y. Wang, C. C. Foster, R. D. Polak, J. Rapaport, and E. J. Stephenson, *Phys. Rev. C* **47**, 2677 (1993).
- [24] J. P. Jeukenne and C. Mahaux, *Nucl. Phys. A* **394**, 445 (1983).
- [25] L. Bimbot, B. Tatischeff, I. Brissaud, Y. Le Bornec, N. Frascaria, and A. Willis, *Nucl. Phys. A* **210**, 397 (1973).
- [26] S. Y. van der Werf, S. Brandenburg, P. Grasdijk, W. A. Sterrenburg, M. N. Harakeh, M. B. Greenfield, B. A. Brown, and M. Fujiwara, *Nucl. Phys. A* **496**, 305 (1989).
- [27] N. Matsuoka, K. Hatanaka, M. Fujiwara, Y. Fujita, T. Saito, K. Hosono, A. Shimizu, M. Kondo, F. Ohtani, H. Sakaguchi, A. Goto, N. Nakanishi, and Y. Toba, *Nucl. Phys. A* **373**, 377 (1982).
- [28] C. M. Vincent and H. T. Fortune, *Phys. Rev. C* **2**, 782 (1970).
- [29] W. S. Gray, R. A. Kenefick, J. J. Kraushaar, and G. R. Satchler, *Phys. Rev.* **142**, 735 (1966).
- [30] F. Pühlhofer, computer code CASCADE; M. N. Harakeh, extended version.
- [31] C. L. Dunford and R. R. Kinsey, NuDat System for Access to Nuclear Data, IAEA-NDS-205, BNL-NCS-65687 (IAEA, Vienna, 1998); information extracted from the NuDat database using the NNDC Online Data Service.
- [32] W. Dilg, W. Schantl, H. Vonach, and M. Y. Uhl, *Nucl. Phys. A* **217**, 269 (1973).
- [33] M. Fujiwara, H. Akimune, I. Daito, H. Fujimura, Y. Fujita, K. Hatanaka, H. Ikegami, I. Katayama, K. Nagayama, N. Matsuoka, S. Morinobu, T. Noro, M. Yoshimura, H. Sakaguchi, Y. Sakemi, A. Tamii, and M. Yosoi, *Nucl. Instrum. Methods Phys. Res. A* **422**, 484 (1999).
- [34] T. Noro, M. Fujiwara, O. Kamigaito, S. Hirata, Y. Fujita, A. Yamagoshi, T. Takahashi, H. Akimune, Y. Sakemi, M. Yosoi, H. Sakaguchi, and J. Tanaka, RCNP Annual Report, 1991 (unpublished), p. 177.
- [35] H. Akimune, I. Daito, Y. Fujita, M. Fujiwara, M. B. Greenfield, M. N. Harakeh, T. Inomata, J. Jänecke, K. Katori, S. Nakayama, H. Sakai, Y. Sakemi, M. Tanaka, and M. Yosoi, *Phys. Rev. C* **52**, 604 (1995).
- [36] K. T. Knöpfle, M. Rogge, C. Mayer-Böricke, J. Pedersen, and D. Burich, *Nucl. Phys. A* **159**, 642 (1970).
- [37] M. R. Cates, J. B. Ball, and E. Newman, *Phys. Rev.* **187**, 1682 (1969).
- [38] A. M. van den Berg, *Nucl. Instrum. Methods Phys. Res. B* **99**, 637 (1995).
- [39] H. J. Wörtche, *Nucl. Phys. A* **687**, 321c (2001).
- [40] S. Rakers, F. Ellinghaus, R. Bassini, C. Bäumer, A. M. van den Berg, D. Frekers, D. De Frenne, M. Hagemann, V. M. Hannen, M. N. Harakeh, M. Hartig, R. Henderson, J. Heyse, M. A. de Huu, E. Jacobs, M. Mielke, J. M. Schippers, R. Schmidt, S. Y. van der Werf, and H. J. Wörtche, *Nucl. Instrum. Methods Phys. Res. A* **481**, 253 (2002).
- [41] H. Fujimura, H. Akimune, A. M. van den Berg, I. Daito, Y. Fujita, M. Fujiwara, M. N. Harakeh, F. Ihara, T. Inomata, K. Ishibashi, J. Jänecke, N. Kalantar-Nayestanaki, H. Kohri, H. Laurent, I. Lhenry, T. O'Donnell, H. K. T. van der Molen, A. Tamii, H. Toyokawa, H. Yoshida, and M. Yosoi, KVI Annual Report, 1997 (unpublished), p. 2.
- [42] F. Ajzenberg-Selove, *Nucl. Phys. A* **523**, 1 (1991).
- [43] D. R. Tilley, H. R. Weller, and C. M. Cheves, *Nucl. Phys. A* **564**, 1 (1993).
- [44] C. M. Baglin, *Nucl. Data Sheets* **86**, 1 (1999).
- [45] G. Finkel, D. Ashery, A. I. Yavin, G. Bruge, and A. Chaumeaux, *Nucl. Phys. A* **217**, 197 (1973).
- [46] G. Finkel, D. Ashery, A. I. Yavin, A. Boudard, G. Bruge, A. Chaumeaux, and M. Rouger, *Phys. Rev. C* **19**, 1782 (1979).
- [47] S. K. Das, A. K. Basak, A. S. Mondal, A. S. B. Tariq, A. F. M. M. Rahman, D. R. Sarker, and H. M. Sen Gupta, *Nuovo Cimento A* **112**, 661 (1999).
- [48] A. Graue, L. H. Herland, K. J. Lervik, J. T. Nesse, and E. R. Cosman, *Nucl. Phys. A* **187**, 141 (1972).
- [49] W. Booth, S. M. Dalglish, K. C. Mclean, R. N. Glover, and F. R. Hudson, *Phys. Lett. B* **30**, 335 (1969).
- [50] M. H. Urin and V. A. Rodin (private communication).